Temperature dependence of the Raman spectrum of orthorhombic Bi_2Se_3

Irene Mediavilla-Martínez,[1] Christian Kramberger,[2] Shabnam Dadgostar,[1] Juan Jiménez,[1]
Paola Ayala,[2] Thomas Pichler,[2] Francisco Javier Manjón,[3] Plácida Rodríguez-Hernández,[4]
Alfonso Muñoz,[4] Nadezhda Serebryanaya,[5] Sergei Buga,[5,6] and Jorge Serrano[1,7,*]
[1]*GdS-Optronlab Group, Department Física de la Materia Condensada, Cristalografía y Mineralogía, Universidad de Valladolid,*
Paseo de Belén 19, 47011 Valladolid, Spain
[2]*Faculty of Physics, University of Vienna, Strudlhofgasse 4, 1090 Wien, Austria*
[3]*Instituto de Diseño para la Fabricación y Producción Automatizada, MALTA-Consolider Team,*
Universitat Politècnica de València, 46022 Valencia, Spain
[4]*Departamento de Física, Instituto de Materiales y Nanotecnología, Universidad de La Laguna, 38205 Tenerife, Spain*
[5]*Technological Institute for Superhard and Novel Carbon Materials, Centralnaya Street 7a, 108840 Troitsk, Moscow, Russian Federation*
[6]*Moscow Institute of Physics and Technology, Institutskiy per. 9, 141700 Dolgoprudny, Moscow Region, Russian Federation*
[7]*Meeting Life LLC, 1210 Washington Avenue, Suite 213, Miami Beach, Florida 33139, USA*

(Received 14 February 2024; revised 20 February 2025; accepted 4 March 2025; published 22 April 2025)

Bismuth selenide, a benchmark topological insulator, grows in a trigonal structure at ambient conditions and exhibits a number of enticing properties related to the formation of Dirac surface states. Besides this polytype, a metastable orthorhombic modification with the *Pnma* space group, o-Bi_2Se_3, has been produced by electrodeposition and high-pressure high-temperature synthesis. It displays significant thermoelectric properties in the midtemperature range, particularly upon Sb doping. However, very little experimental information is available on the fundamental properties of this orthorhombic polytype, such as, e.g., the electronic band gap and the lattice dynamics. Here we report the temperature dependence of the Raman spectra of o-Bi_2Se_3 between 10 K and 300 K, which displays an anharmonic behavior of the optical phonons that can be modeled with a two-phonon decay channel. To analyze the data, we performed *ab initio* calculations of the electronic band structure, the phonon frequencies at the center of the Brillouin zone, and the phonon dispersion relations along the main symmetry directions, examining the effect of spin-orbit coupling in both phonon and electronic energies. Lastly, we report cathodoluminescence experiments at 83 K that set a lower limit to the electronic band gap at 0.835 eV, pointing to an indirect nature, in agreement with our calculations. These results shed light on the essential properties of orthorhombic Bi_2Se_3 for further understanding of the potential of this semiconductor for thermoelectrics and other relevant applications.

DOI: 10.1103/PhysRevB.111.134304

I. INTRODUCTION

The quest for advanced materials with tailored applications has been paved with the discovery of fascinating properties, sometimes unexpectedly. One of the benchmark examples of this combination of new physics and enticing applications is the case of bismuth selenide, with a trigonal ($R\bar{3}m$) tetradymite structure, α-Bi_2Se_3, a three-dimensional topological insulator, i.e., a material characterized by an insulating bulk and conducting surface states. With a single Dirac cone on the Fermi surface [1], α-Bi_2Se_3 exhibits spin-momentum locking of massless helical Dirac fermions [2], due to strong spin-orbit coupling (SOC), coexisting with a two-dimensional electron gas [3], and Landau quantization of the surface states [4]. Trigonal Bi_2Se_3 has been suggested to exhibit superconducting behavior, demonstrated with Cu doping [5]. In nanoribbons, it presents pronounced Aharonov-Bohm oscillations in magnetoresistance [6] that point to potential applications in future spintronic devices at room temperature. More recently, charge-current-induced spin polarization has been detected electrically in α-Bi_2Se_3 films [7] due to locking of spin-momentum using a ferromagnetic metal tunnel barrier surface contact to measure voltage. This opens a pathway to control spin state population for potential applications in quantum computing. Moreover, α-Bi_2Se_3 films have been shown to generate a spin-transfer torque on adjacent ferromagnetic thin films [8], implying that topological insulators could facilitate efficient electrical manipulation of magnetic materials at room temperature, for example, in logic and memory applications. Coupling α-Bi_2Se_3 with a ferromagnetic insulator in a bilayer system, such as EuS, has also been shown to demonstrate topologically enhanced ferromagnetism persisting up to room temperature, due to proximity coupling [9], highlighting further the potential for these applications. High-performance large-area electronics is another arena where α-Bi_2Se_3 has been proposed for applications, together with 2D materials such as WSe_2, $NbSe_2$, In_2Se_3, Sb_2Te_3, and black phosphorus [10].

Despite this broad range of applications, thermoelectric properties are much less appealing in α-Bi_2Se_3 than in its heavier analog, Bi_2Te_3. With similar trigonal structure, Bi_2Te_3

---

[*] Contact author: jorge.serranogutierrez@gmail.com

is known to display superior thermoelectric properties at room temperature due to the presence of six valleys for the highest valence band in the electronic band structure versus only one available in α-Bi_2Se_3 [11]. This, combined with challenges to achieve p-type doped α-Bi_2Se_3, due to natural Se vacancy dominant defect chemistry, make potential thermoelectric applications only of interest at low temperatures [12] or in $Bi_2Te_xSe_{1-x}$ alloys [13].

There is, however, another polytype of Bi_2Se_3 with an orthorhombic phase, labeled hereafter as o-Bi_2Se_3, metastable at ambient conditions, that seems to qualify better than its trigonal counterpart for thermoelectric effects [14]. This polytype has displayed recent applications in a simultaneous heat flux and temperature acquisition dual-mode sensor [15]. The Bi_2Se_3 trigonal-to-orthorhombic phase transition has shown applications in metal-dielectric-metal metamaterials with tunable negative refractive index in the near-infrared spectral region [16]. Furthermore, o-Bi_2Se_3 has been proposed as a promising candidate for photovoltaic interfaces due to an excellent band energy alignment with usual photovoltaic substrates, such as TiO_2 [17]. Phase analysis and knowledge of phase transitions are essential in discovering applications of materials, sometimes achieved in metastable phase, as is the case of o-Bi_2Se_3, and sometimes in 2D and nanostructures, such as graphene or wurtzite GaP, respectively. The latter, for example, holds the promise of direct band light emission at 550–570 nm, the so-called green-yellow band, only available in nanowires [18], whereas zincblende GaP is an indirect band-gap semiconductor.

With *Pnma* space group, o-Bi_2Se_3, naturally present as a mineral named guanajuatite [19], displays quasi-one-dimensional atomic ribbons [20] and can be produced by quenching it from high-pressure high-temperature growth conditions [21,22] and by electrodeposition of thin films using electrochemical atomic layer epitaxy [23].

Despite the technological interest, o-Bi_2Se_3 has received much less attention from the experimental viewpoint compared to its trigonal counterpart, and many fundamental properties, such as the electronic band gap, its direct or indirect nature, and the lattice dynamics properties, such as phonon dispersion relations, Raman spectra, and their dependence with pressure and temperature, are yet to be fully ascertained.

We report here an investigation of the temperature dependence of the Raman spectrum of o-Bi_2Se_3 combined with first-principles electronic and lattice dynamics calculations. The role of the anharmonicity, predicted to be larger in orthorhombic than in trigonal Bi_2Se_3, is also discussed, as well as the strength of the electron-phonon coupling, indicated by the zero-temperature renormalization of the Raman modes. Moreover, we report here cathodoluminescence data at 83 K that enable us to provide a lower estimate of the experimental electronic band gap, of 0.835 eV, in excellent agreement with the electronic band-structure calculations.

These results pave the way to further experimental work toward elucidating the role of the lattice potential anharmonicity in the thermal transport, electronic, and optical properties of o-Bi_2Se_3.

The paper is organized in the following way: Section II describes the sample preparation, the experimental methods of both Raman and cathodoluminescence (CL) measurements, and the details on the *ab initio* calculations employed for the analysis. Section III contributes the observations made in light of the different experiments and calculations and provides the background for the analysis of the anharmonicity of the Raman modes. This analysis is reported in Sec. IV. The results are summarized in Sec. V and additional complementary information is provided in the Supplemental Material (SM) [24].

TABLE I. o-Bi_2Se_3 atomic parameters obtained from the refinement of XRD spectrum given in Fig. SM.1 in the Supplemental Material [24]. The experimental lattice parameters obtained from the fit were $a = 11.7936$ Å, $b = 4.1041$ Å, and $c = 11.5724$ Å.

Atom	Site	x	y	z
Bi	Bi1	0.01332	0.25000	0.32957
Bi	Bi2	0.34599	0.25000	0.54081
Se	Se1	0.05123	0.25000	0.86597
Se	Se2	0.88154	0.25000	0.55105
Se	Se3	0.22378	0.25000	0.19475

II. METHODS

A. Sample preparation

The commercially available high purity (99.999%, Aldrich) α-Bi_2Se_3 powder was used for high-pressure high-temperature synthesis of o-Bi_2Se_3 in a toroid-type apparatus at $P = 4$ GPa, $T = 673$ K. A powder sample with a 5 mm diameter and 3 mm height was wrapped in tantalum foil and placed inside a graphite heater, and then inside a lithographic limestone container. The heating rate was 20 K s^{-1}. The temperature holding time under pressure was 60 s, and the cooling rate was 200 K s^{-1} to quench the structure of the high-pressure phase. After cooling down to room temperature, pressure was gradually released, obtaining several sintered powder polycrystalline samples. More details about the synthesis process have been reported in Ref. [25], that also reports information on a metastable phase with orthorhombic crystal structure, *Fdd2* space group, of Bi_2Se_3. The x-ray diffraction pattern of o-Bi_2Se_3 is provided in Fig. SM.1 in the Supplemental Material [24]. We used an Empyrean Panalytical x-ray diffractometer with Cu Kα radiation and an ultrafast high-sensitive x-ray area detector PIXcel3D. The diffractograms were fitted by Rietveld profile-matching using the FULLPROF program [26]. At each refinement cycle, the fractional coordinates, scale factor, isotropic thermal parameters, profile function, and cell parameters were optimized. Its unit cell parameters are $a = 11.794$ Å, $b = 4.1041$ Å, and $c = 11.574$ Å. The atomic parameters resulting from the the Rietveld fit are provided in Table I.

B. Experiments

CL experiments were conducted at 80 K, employing a LEO 1530 Carl Zeiss field-emission scanning electron microscope (SEM) equipped with a MonoCL 2 Gatan UK CL system. Detection was performed with a Peltier-cooled InGaAs detector optimized to work between 900 nm (1.38 eV) and 1800 nm (0.69 eV). An aperture of 60 µm and an electron beam energy of 20 keV were selected for this experiment. The sample was

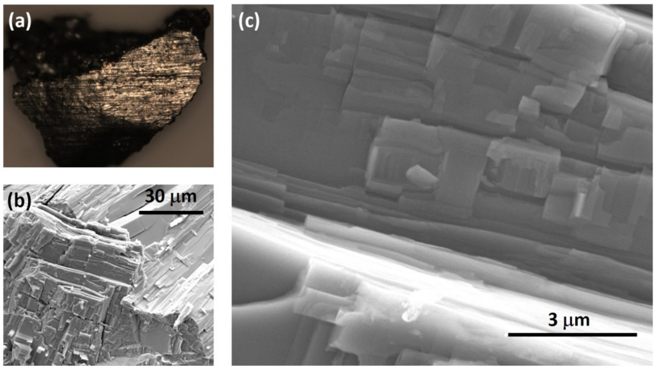

FIG. 1. (a) Optical image of the sample under investigation and (b), (c) SEM images of o-Bi_2Se_3 at different magnifications, displaying a stratified structure congruent with an orthorhombic cell.

mounted on a copper holder and contacted with a copper wire to reduce the electron-beam induced charge accumulation on the surface. Temperature was controlled by adjusting the flow of liquid nitrogen to the cold finger in thermal contact with the sample holder, and by activating a heater equipped with a feedback control loop. In this way, the CL spectrum was acquired at 83 K with an accuracy of 1 K at sample stage.

Raman experiments were undertaken in the same sample in the 10 K–300 K temperature range, employing a Horiba T64000 triple grating spectrometer and a dye laser of 594 nm excitation line. Spectra were acquired using a liquid nitrogen cooled CCD detector. The spectral resolution was better than 1 cm^{-1}, as determined from a Gaussian fit of the spectrum of Ne lines. Power was kept below 1 mW to avoid a temperature-induced phase transformation by laser heating [27]. The sample, displayed in Fig. 1(a), was kept in a liquid He flow cryostat during the experiment and temperature was read using a PT100 sensor.

C. *Ab initio* calculations

Ab initio zero-temperature total-energy simulations were carried out within the framework of density functional theory (DFT) [28] as implemented in the VIENNA AB INITIO SIMULATION PACKAGE [29], VASP, using projector augmented-wave pseudopotentials [30,31]. A plane-wave energy cutoff of 380 eV was employed to ensure accurate converged results. The *k*-point sampling of the Brillouin zone (BZ) was performed using a $6 \times 14 \times 6$ dense grid to ensure high convergence in the integration over the BZ. The exchange-correlation energy was described using the generalized gradient approximation (GGA) with the Perdew-Burke-Ernzerhof functional [32], including the dispersive corrections using the Grimme DFT-D3 method [33]. Spin-orbit coupling was taken into account in the band-structure calculations, which were obtained with and without including this term. The high symmetry path was chosen using the SEEK-PATH utility [34]. The unit cell parameters and the atomic positions were fully relaxed imposing that the forces on the atoms were less than 0.003 eV/Å and the deviations of the stress tensors from a diagonal hydrostatic form were lower than 0.1 GPa. These conditions resulted in $a = 11.852$ Å, $b = 4.160$ Å, and $c = 11.561$ Å, in good agreement with the experimental values reported in the literature, e.g., by Ref. [35], of 11.71, 4.11, and 11.43 Å, respectively, and with the results we obtained by XRD, mentioned above.

TABLE II. Calculated electronic band-gap energy, in meV, for *Pnma*-type Bi_2Se_3 obtained with and without including spin-orbit coupling (SOC), and peak energy observed in CL spectrum at 83 K.

	Direct gap	Indirect gap
Exp. (CL data)		835(10)
Without SOC	974	948
With SOC	624	601
Other DFT	900[a], 1100[b], 990[c]	860[c]
GW with SOC	910[c]	

[a] Reference [37],
[b] Reference [38],
[c] Reference [39].

Lattice-dynamic calculations of the phonon modes were carried out at the zone center (Γ point) of the BZ with the PHONOPY package [36]. These calculations provide not only the frequency of the normal modes but also their symmetry and polarization vectors. This allows us to identify the irreducible representations and the character of the phonon modes at the Γ point. A $4 \times 4 \times 4$ supercell was used to obtain the phonon dispersion and the phonon density of states.

III. RESULTS

Figure 1(a) displays the optical image of the sample under investigation. Figures 1(b) and 1(c) show SEM images obtained with 20 keV electron beam energy at several magnifications. A stratified structure is observed at the micro- and submicron scale, with *a*-*c* planes piled on top of each other. The sample has a shiny metalliclike luster that already indicates an electronic band gap with an energy below the visible range.

A. Electronic band structure and band gap

The CL spectrum taken at 83 K is shown in Fig. 2(a), revealing a low-signal broad band peaked at 1484 nm (0.835 eV) and a higher energy edge at 1367 nm (0.907 eV). Reported optical absorption experiments using near-infrared light on *Pnma* Bi_2Se_3 obtained by electrodeposition revealed a potentially direct energy band gap, varying between 0.9 eV for 0.5 μm thick films to 1.25 eV for the thickest films, suggesting their potential for photovoltaic applications [35]. Our estimate for the band-gap energy is consistent with this range. To shed more light on the nature of this CL band, we calculated the electronic band structure of o-Bi_2Se_3. This is displayed in Fig. 2(c) along the main symmetry directions of the BZ, indicating with red dashed and black solid lines the electronic bands obtained with and without including SOC effects, respectively.

As a general trend, taking into account SOC effects results in lower conduction band energies and a narrowing of the band gap. These calculations predict an indirect nature of the band gap, located between a maximum of the valence band (VB) along the Γ-Z direction and a minimum of the

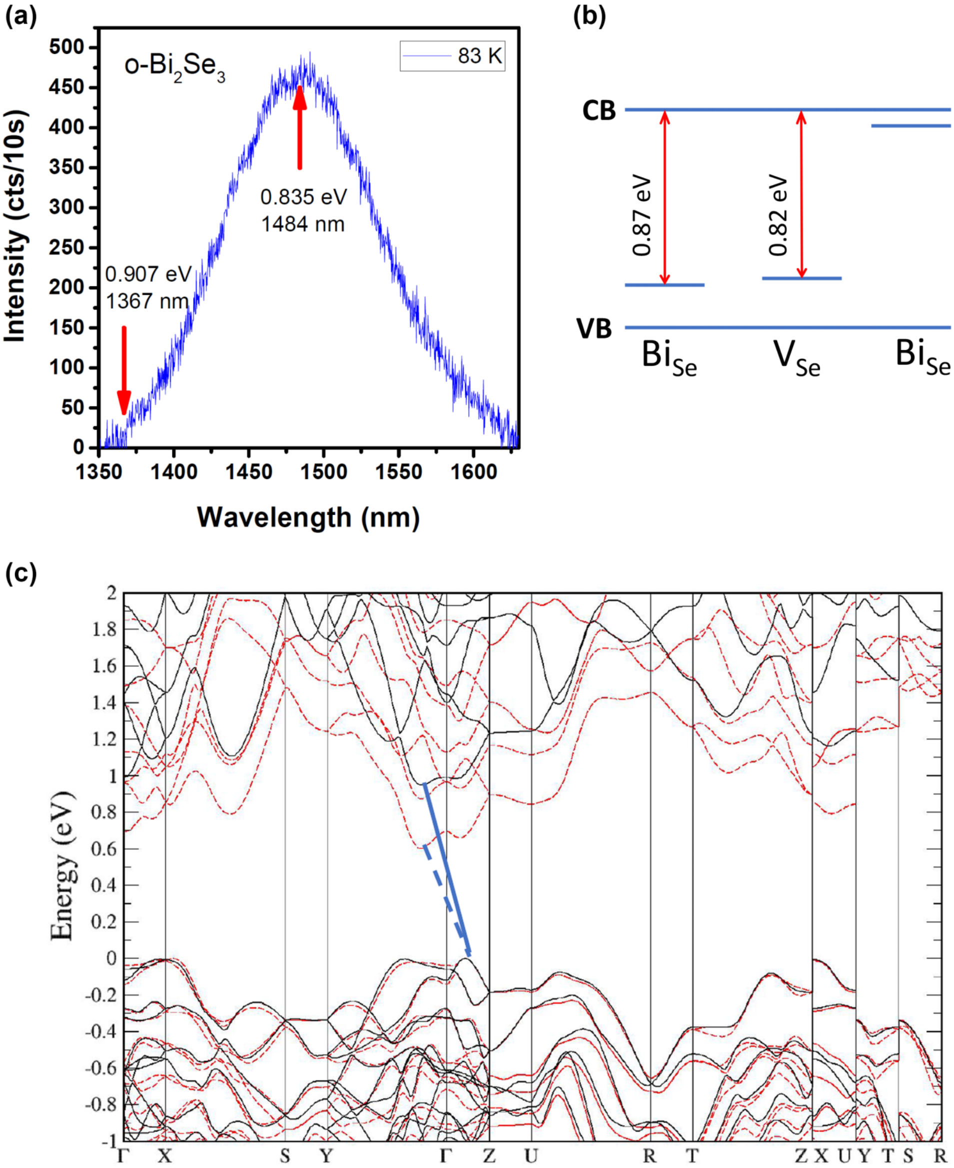

FIG. 2. (a) CL spectrum at 83 K of o-Bi$_2$Se$_3$ at the point marked in the SEM image of Fig. 1(b). (b) Schematic band structure displaying the top valence band (VB), the bottom conduction band (CB), and three defect energy levels corresponding to donor levels at Bi$_{Se}$ antisites and Se vacancies, and acceptor levels corresponding to the same antisites. Energy values taken from Ref. [17]. (c) Calculated *ab initio* electronic band structures for o-Bi$_2$Se$_3$ along the main symmetry directions of the Brillouin zone with (red dashed lines) and without (black solid lines) including SOC effects. The straight lines display the indirect band gap obtained in both calculations.

conduction band (CB) along the Γ-Y direction. Table II displays the values of the calculated direct and indirect electronic band gap of orthorhombic Bi$_2$Se$_3$ with and without including SOC effects. For the sake of completeness, our data are compared with those stemming from similar DFT and *GW* calculations [37–39]. One can argue that, due to the common trend of band-gap energy understimation by DFT-GGA calculations, this prediction may be incorrect. However, adding a scissor operator would rigidly shift all electronic bands without affecting the indirect nature of the lowest band gap. Furthermore, this indirect nature revealed by our calculations, both with and without SOC, is in agreement with predictions made by Ref. [39].

The calculated band gap energy difference between direct and indirect gaps, however, amounts to 0.1–0.2 eV, which makes it challenging to ascertain the true nature of the gap. Variations on the lattice parameters results in significant changes in the calculated band gap energy [39], e.g., up to 0.3 eV, between the values obtained using the experimental lattice constants and those corresponding to DFT fully optimized ones. This fact also prevents the determination of the direct or indirect nature of the band gap based solely on the calculated data. Cathodoluminescence data show a very weak signal at low temperature, that suddenly vanishes with increasing temperature to 90 K. This behavior is consistent with defect-related luminescence bands and makes us attribute the band gap to indirect transitions from the VB to the CB. If we had a direct band gap, a much larger CL signal would be expected and lasting until higher temperatures. After repetition of the experiment several times in different polycrystals

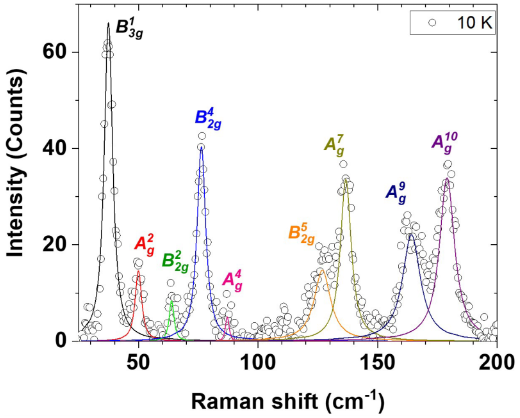

FIG. 3. Raman spectrum of o-Bi_2Se_3 at 10 K (symbols). The lines display fits with a Voigt profile, taking into account the experimental resolution (approx. 1 cm^{-1}). The labels display the assigned mode symmetry.

of the same batch, only this weak signal at 83 K was observed. We therefore conclude that an indirect band gap with some defect bands is the most plausible scenario describing our experimental findings.

Tumelero *et al.* [17] reported a calculated band gap energy of 1.2 eV and their comprehensive DFT study of the main defect energy levels on o-Bi_2Se_3 found donor-type defect levels at 0.84 eV and 0.82 eV from the bottom of the CB corresponding to Bi_{Se} antisite and Se vacancies, respectively. These levels are in agreement with the peak energy of the CL spectrum, located at 0.835 eV. Figure 2(b) displays a schematic diagram of the potential transitions between these defect bands and both the VB and the CB to illustrate the possible origin of the features in the CL spectrum. Assuming a band gap energy of 0.91 eV according the most accurate *GW* calculations with SOC effects [39], an alternative explanation for this peak would be a transition from acceptor states linked to a Bi_{Se} antisite with a calculated activation energy of 0.09 eV [17]. This scenario matches as well with the peak energy of detected CL signal, 0.835 eV, that can be taken as an experimental low energy estimate for the electronic band gap.

B. Raman phonon frequencies at low temperature

Figure 3 shows the Raman spectrum of o-Bi_2Se_3 obtained at 10 K. Several peaks appear in the spectrum and are attributed to different modes, the symmetry indicated in the figure. The highest energy mode peaks at about 170 cm^{-1}. To the best of our knowledge, only one work has previously reported the o-Bi_2Se_3 Raman spectra recently for temperatures between 300 K and 570 K [40]. However, anharmonic effects are expected to be significant at those temperatures given the relatively low energy of the o-Bi_2Se_3 phonon modes. A precise determination of these anharmonic effects therefore requires us to investigate the temperature dependence of the Raman spectra from 10 K up to room temperature and above.

C. Temperature dependence of the Raman spectrum

Figure 4(a) plots the Raman spectra at selected values in the 10–300 K temperature range. Some general trends are apparent: (i) Phonon frequencies shift toward lower values with increasing temperature, as expected from the activation of third- and high-order anharmonic decay channels, (ii) this shift is larger for higher frequency modes, and (iii) Raman peaks broaden and Raman intensities tend to decrease with increasing temperature, with a couple of exceptions, also in alignment with an increasing anharmonicity and thereby reduced phonon lifetime. Since the Raman spectra were taken in a polycrystalline sample, we attribute intensity fluctuations and the appearance of additional peaks to changes in the laser spot position when the sample temperature is increased.

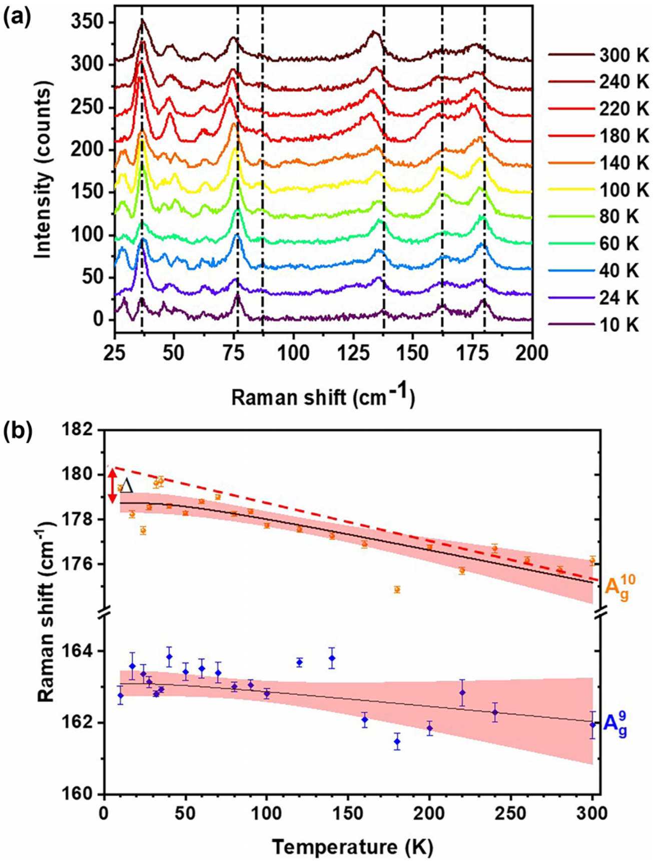

FIG. 4. (a) Selected Raman spectra of o-Bi_2Se_3 as a function of temperature from 10 K to 300 K. The vertical lines are guides to the eye that display the shift of the most intense modes observed at 10 K upon increase of temperature. (b) Temperature dependence of the two highest frequency modes of o-Bi_2Se_3 and fit (solid lines) with Eq. (1). The dashed line displays the extrapolation at $T = 0$ K of the high temperature linear behavior for the highest frequency mode, yielding the zero-temperature phonon renormalization Δ. Color bands have been used to show the 99% confidence interval [64].

A Voigt profile was used to fit the peaks in the Raman spectra. This profile results from the convolution of an intrinsic Lorentzian profile for the phonon excitation and a Gaussian function to take into account the spectrometer resolution function, the latter with a full width at half maximum of 1 cm^{-1}.

As anharmonic effects are typically more visible for the high energy modes, we display in Fig. 4(b) the Raman shift of the upper two modes as a function of temperature. The Raman shift of some of the lowest energy modes is provided as well in Figs. SM.2, SM.3, and SM.4 in the Supplemental Material [24].

IV. ANALYSIS

Pnma-type Bi_2Se_3 has an orthorhombic cell with 20 atoms per unit cell, thus yielding a rather complex map of phonon dispersion relations with 60 different phonon branches, similar to Sb_2S_3 and Sb_2Se_3 [41,42]. Group theory predicts 60 vibrational modes at the BZ center whose irreducible representations are $\Gamma = 10B_{1u} + 5B_{2u} + 10B_{3u} + 5B_{1g} + 10B_{2g} + 5B_{3g} + 5A_u + 10A_g$, where B_{1g}, B_{2g}, B_{3g}, and A_g modes correspond to Raman-active modes, B_{1u}, B_{2u}, and B_{3u} modes correspond to infrared-active modes, A_u modes are silent, and 1 B_{1u}, 1 B_{2u} and 1 B_{3u} modes are acoustic modes. This leads to 30 Raman-active modes and 22 infrared-active modes.

The lattice dynamics of its trigonal counterpart, with $R\bar{3}m$ space group, α-Bi_2Se_3, is considerably simpler, as the crystal lattice has five atoms in the primitive unit cell. Therefore, only 15 vibrational modes appear at the BZ center [43,44]. The irreducible representations for the zone-center modes in this case are $\Gamma = 2A_{1g} + 3A_{2u} + 2E_g + 3E_u$, where A_{1g} and E_g modes are Raman active, A_{2u} and E_u modes are infrared active, E_u and E_g are doubly degenerated, and one A_{2u} and one E_u modes correspond to the acoustic phonons. There are, hence, four Raman-active modes, $2A_{1g}$ and $2E_g$, that are observed at 39 cm^{-1} (E_g), 71.5 cm^{-1} (A_{1g}), 132.5 cm^{-1} (E_g), and 174 cm^{-1} (A_{1g}) at room temperature and ambient pressure [43,45,46]. The o-Bi_2Se_3 primitive cell also has five atoms, however, the orthorhombic unit cell displays two inequivalent Bi_2Se_3 ribbons with two unit formulas each, which lead to the need to take 20 atoms into consideration for the lattice dynamics.

The Raman modes of trigonal Bi_2Se_3 have been the subject of intense investigation since the pioneering work by Richter *et al.* in 1977 [47], addressing both bulk single crystals [48–51], few epitaxial layers [45,52–54], thin films [55], and nanoplates [56,57]. Several studies report the temperature dependence of these modes at different temperature ranges [46,49,56,58]. Effects of pressure [43,44] and magnetic field dependence [46] have also been investigated in the past. The lattice dynamics of orthorhombic *Pnma* Bi_2Se_3, on the contrary, has received attention only very recently [40].

Figure 5(a) displays the calculated phonon dispersion relations along the main symmetry directions of o-Bi_2Se_3, whereas Fig. 5(b) shows the total, and Bi- and Se-projected partial one-phonon density of states (DOS). As expected, the higher frequency modes are dominated by displacements of the Se sublattice. The Van Hove singularities of the one-phonon DOS are expected to play a role in the peak broadening of the Raman spectra of alloys of o-Bi_2Se_3, as, for example, in thermoelectric materials such as in orthorhombic $Bi_2Te_xSe_{3-x}$, due to disorder-induced breakdown of momentum conservation. The frequencies corresponding to the main Van Hove singularities are listed in Table III.

From the 30 Raman-active modes of o-Bi_2Se_3, only around ten modes can be identified due to several factors: a large anharmonic broadening, much weaker signal for B_g modes, the spectral resolution of 1 cm^{-1}, and the polycrystalline character of the sample under investigation. Furthermore, the spectra acquisition took over an hour per spectrum, which led to fluctuations of the 1 μm diameter laser spot on the sample. This led to changes in Raman intensity for some of the modes as a function of temperature that can be attributed to change in the polycrystal orientation under observation. A similar number of Raman-active modes were previously measured

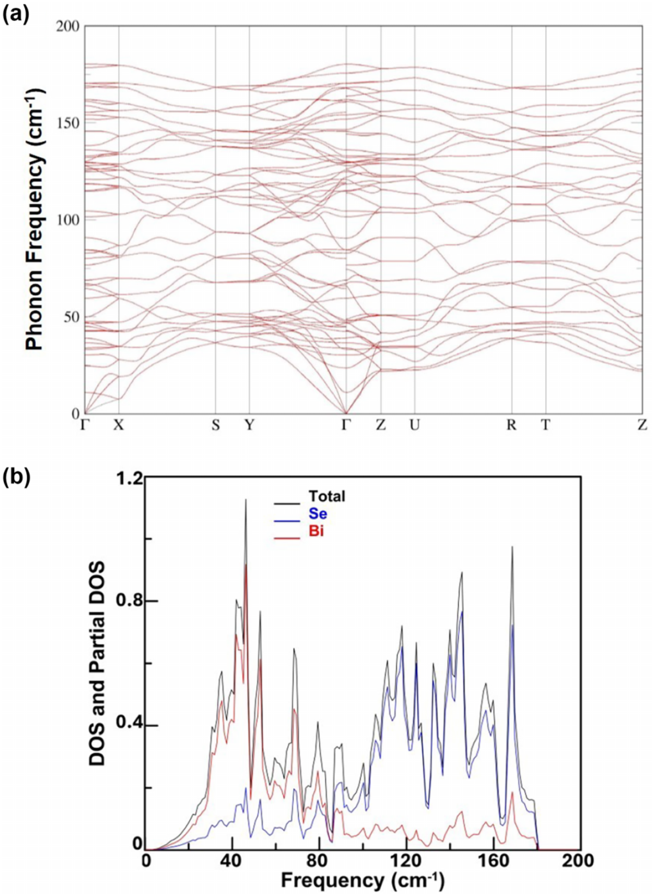

FIG. 5. *Ab initio* (a) phonon dispersion relations of o-Bi_2Se_3 along the main symmetry directions; (b) total (black), Bi- (red), and Se-projected (blue) one-phonon density of states.

TABLE III. Calculated frequencies of the main Van Hove singularities of the one-phonon DOS and the corresponding assignments in light of the *ab initio* phonon dispersion relations.

ω (cm^{-1})	DOS	Assignment	ω (cm^{-1})	DOS	Assignment
31	0.40	ΓX	111	0.61	SY,RT
35	0.58	ΓX,ZU	118	0.72	RT
43	0.80	RT	124	0.67	UR
46	1.13	ΓX,SY	132	0.60	ZUR
53	0.77	UR	143	0.73	ΓZ
68	0.65	SY	145	0.89	ΓY
79	0.41	SY,ZU	156	0.54	ΓX
90	0.34	SY, ΓZ	160	0.48	ΓZ
100	0.28	RT	169	0.98	ΓX
107	0.41	ZU	178	0.17	ΓX

at room conditions for other *Pnma*-type related compounds: Sb_2Se_3, up to 250 cm^{-1} [41]; Bi_2S_3, up to 300 cm^{-1} [59]; and Sb_2S_3, up to 350 cm^{-1} [42,60].

Figure 4(b) shows a fit to the experimental phonon frequencies with a two-oscillator model assuming anharmonic decay into two modes of equal energy ω_1. This is the so-called Klemens' ansatz [61], given by Eq. (1):

$$\begin{aligned}\omega &= \omega_0 - \Delta[1 + 2n_{\mathrm{BE}}(\omega_1, T)]\\ &= \omega_0 - \Delta\left[1 + \frac{2}{e^{\frac{\hbar\omega_1}{k_B T}} - 1}\right],\end{aligned} \tag{1}$$

where ω_0 is the unrenormalized zero-temperature phonon energy, Δ is the energy renormalization at 0 K, n_{BE} is the Bose-Einstein function, and $\hbar$ and k_B are Planck's and Boltzmann's constants, respectively. Notice that ω_1 is a phonon frequency lower than ω_0.

Energy conservation must be fulfilled for anharmonic decay. This is reflected in the rule $\omega_0 = \omega_1 + \omega_2$ for the allowed transitions in the calculation of the second-order anharmonic contributions to the phonon linewidth. However, in the calculation of the same contribution to the phonon frequency shift, a Kramers-Kronig transformation must be applied, mixing decay channels that are not required for energy conservation. This is explicitly displayed in the exact equations corresponding to the third-order anharmonic contributions to the phonon shift and linewidth, provided by Eqs. (2.14a) and (2.15a) in Ref. [62] for silicon, and it also holds for binary and multinary compounds [63]. Note that the delta functions in Eqs. (2.14) and (2.15) [62], responsible for energy conservation, appear only in the expressions of the anharmonic contributions to the linewidth. Hence, ω_1 may be taken as an adjustable independent parameter.

To simplify the number of fitted parameters, we have imposed $\omega_1 = \omega_0/2$. The quality of the fit can be assessed using 99% confidence intervals as defined in Ref. [64]. These are displayed in Fig. 4(b) and further figures using a colored band. Unfortunately, the quality of the data prevents extracting additional information on other decay channels, e.g., such as the electron-phonon contribution in related materials with topological insulators (Ref. [65]).

Since *ab initio* phonon frequencies are usually obtained within the harmonic approximation, comparison between experimental and calculated Raman frequencies is more accurate and appropriate using the values obtained for ω_0 rather than the experimental ω values at low temperature. Investigation of anharmonicity using *ab initio* simulations requires much more complex calculations, similar to those reported in the pioneering work of Debernardi *et al.* in Ref. [66], and it is beyond the scope of this paper.

In the high temperature limit, $n_{\mathrm{BE}}(\omega, T) \approx \hbar\omega/(k_B T)$. From this limit, together with Eq. (1), we can calculate the slope of the temperature dependence of the Raman phonons at the high temperature range. Given the relatively low Raman frequencies of o-Bi_2Se_3, one can safely assume that at room temperature we are in this high T regime, and then

$$\frac{\partial\omega}{\partial T} \approx -4\frac{k_B\Delta}{\hbar\omega_0}. \tag{2}$$

Table IV displays the calculated Raman frequencies both with and without taking into account SOC effects, with the values of ω_0 and Δ derived from our experimental results, the Raman frequencies obtained at 300 K, and those reported in Ref. [40]. We also report here the high temperature limit of the temperature derivative of the Raman phonon frequencies, as calculated with Eq. (2). Another estimate for the temperature derivative at room temperature can be obtained by using the approximation $\frac{\partial\omega}{\partial T} \approx (\omega_{300\mathrm{K}} - \omega_0)/300$. In this case, much lower values are obtained, e.g., for the highest frequency modes, an average temperature derivative of -0.012 and -0.014 cm^{-1} K^{-1}, similar to those reported for trigonal Bi_2Se_3 modes (between -0.012 and -0.024 cm^{-1} K^{-1}) [56,67,68]. The values of Δ give information about the zero-temperature renormalization of the phonon frequency and are typically larger the more anharmonic the material. Note that in Table IV only the largest energy mode displays significant renormalization, 2.1 cm^{-1}, the value being comparable to those reported for isotopic CuI, 2.0–2.6 cm^{-1}, a prototypical anharmonic semiconductor with similar value for the highest-frequency Raman mode [63].

We can, therefore, conclude that the anharmonic effects are significant in this material. However, the anharmonicity seems to be lower than that exhibited by trigonal Bi_2Se_3. The latter presents both larger linewidths of the Raman peaks and an overshooting at 50 K of the higher A_{1g} Raman frequency as a function of temperature, indicating phonon interactions with the electronic system beyond the expected anharmonic decay [46]. Figure 6(a) displays the phonon linewidth for the A_g^9 mode, with $\omega_0 = 164.8$ cm^{-1}. Significant data scattering is observed and attributed to a varying mixture of mode intensities due to the fluctuations of the laser spot in the sample at different temperatures. Unfortunately, for o-Bi_2Se_3 the large number of Raman modes in a relatively small frequency range challenges a thorough analysis of the anharmonicity through direct investigation of the phonon linewidths as a function of temperature. Despite this overlap, we were able to evaluate the temperature dependence of the linewidth of two other modes, B_{2g}^4 and A_g^{10}, corresponding to bare frequencies $\omega_0 = 76$ cm^{-1} and 180 cm^{-1}, displayed in Figs. 6(c) and 6(b), respectively.

The anharmonic contribution to the phonon linewidth, Γ_{anh} (FWHM), is related to the phonon frequency shift due to anharmonic decay, Δ, by a Kramers-Kronig transformation, since both correspond to the real and imaginary parts of the phonon self-energy $\Sigma(\omega)$ [62]:

$$\Sigma(\omega) = \Delta(\omega) - i\frac{\Gamma_{\mathrm{anh}}(\omega)}{2}, \quad \text{where using the Klemens' ansatz,}$$

$$\begin{aligned}\Gamma_{\mathrm{anh}} &= \Gamma_1[1 + 2n_{\mathrm{BE}}(\omega_1, T)]\\ &= \Gamma_1\left[1 + \frac{2}{e^{\frac{\hbar\omega_1}{k_B T}} - 1}\right].\end{aligned} \tag{3}$$

To describe properly the experimental phonon linewidths, we need to introduce an additional broadening, Γ_0, that takes into account crystalline disorder effects and other phonon scattering sources such as defects. This term may account for fluctuations due to experimental errors as well.

TABLE IV. Calculated and measured Raman frequencies for o-Bi_2Se_3 for different symmetry modes. The unrenormalized phonon frequencies, ω_0, and their renormalization at 0 K, Δ, extracted from the experimental data using Eq. (1), are also displayed here. Raman frequencies are given in cm^{-1}, and temperature derivatives were calculated from the experimental data using Eq. (2). Experimental frequencies are given at 300 K except for some modes that were not observed at room temperature. In those cases, the temperature at which they are observed is indicated with a superscript.

		Theory, ω_0		Experiment				Ref. [40]
Mode	Symmetry	With SO	No SO	ω_0	Δ	ω(300 K)	$\frac{\partial\omega}{\partial T}\left(\frac{cm^{-1}}{K}\right)$	ω(300 K)
1	B^1_{2g}	30.7	31.1	28.85(15)	0.04(2)	28.4^{280K}	−0.004	
2	B^1_{1g}	30.7	31.7					
3	A^1_g	32.7	34.2					
4	B^1_{3g}	34.2	35.4	36.7(2)	−0.05(3)	37.3	0.004	
5	B^2_{1g}	44.9	46.4	45.4(9)	−0.2(2)	48.4	0.012	
6	B^2_{3g}	45.7	47.3					
7	A^2_g	45.7	47.0	50.5(6)	0.0(2)	50.6^{140K}	0.000	
8	A^3_g	58.3	59.9					
9	B^2_{2g}	64.6	67.2	63.37(15)	0.06(4)	63.0	−0.003	
10	B^3_{2g}	67.1	69.0					
11	B^4_{2g}	80.4	82.6	76.6(3)	0.46(9)	74.9	−0.017	
12	A^4_g	82.4	84.6	88.2(10)	1.7(4)	78.3	−0.054	
13	B^3_{1g}	98.6	101.3					
14	B^3_{3g}	102.1	104.5					
15	B^5_{2g}	111.9	114.0					109.0
16	A^5_g	112.1	115.0					
17	A^6_g	115.7	117.3					
18	B^6_{2g}	118.7	121.7					
19	B^4_{3g}	120.4	124.9					
20	B^4_{1g}	124.1	128.4	127.3(12)	−0.1(7)	129.5	0.002	126.6
21	A^7_g	128.1	130.1	137.6(4)	1.4(2)	134.0	−0.028	
22	B^5_{1g}	128.7	132.8					
23	B^5_{3g}	131.4	135.4					
24	B^7_{2g}	142.5	145.7					141.1
25	B^8_{2g}	148.7	151.7					
26	A^8_g	151.0	153.7					
27	A^9_g	158.2	161.2	164.8(4)	1.2(3)	161.1	−0.020	158.7
28	B^9_{2g}	163.4	168.5					
29	A^{10}_g	167.0	170.6	180.5(4)	2.1(3)	176.2	−0.032	173.0
30	B^{10}_{2g}	167.4	170.3					

If we modify Eq. (3) to introduce this broadening, we can fit the linewidths with the following equation [69]:

$$\Gamma = \Gamma_0 + \Gamma_1[1 + 2n_{BE}(\omega_1, T)]. \tag{4}$$

Equation (4) provides a good fit in some cases, as in Fig. 6(a), dotted line, where disorder and defect effects dominate. However, as Menéndez and Cardona showed for crystalline Si [70], in other cases Klemens' ansatz falls short of explaining the observed temperature dependence of Raman phonon linewidths due to an excessive weight of overtone modes and lack of consideration of other two-phonon combinations as anharmonic decay channels, respecting momentum and energy conservation rules, such as $q_1 = -q_2$ and $\omega_0 = \omega_1 + \omega_2$.

The generalized expression for Eq. (4) including decay into two modes with different frequencies is then given by

$$\Gamma = \Gamma_0 + \Gamma_1[1 + n_{BE}(\omega_1, T) + n_{BE}(\omega_2, T)], \tag{5}$$

and it has been used in the literature to properly describe the temperature dependence of Raman phonon linewidths for other diatomic semiconductors, such as CuI [63].

In Figs. 6(b) and 6(c), a sudden increase in linewidth is observed below 100 K, followed by a more moderate increase at higher temperatures. This peculiar behavior may have two distinct causes: (i) Either it is a signature of a strong anharmonicity for o-Bi_2Se_3 or (ii) it is an effect of a large disorder component in the linewidth added to a moderate anharmonic term. In the first case, the observed trend requires the use of Eq. (5) to be accounted for properly, whereas the second case can be explained employing the simpler Klemens' expression, Eq. (4). Confidence intervals have been used with fits employing each equation to compare the quality of both hypotheses and are displayed with red and blue bands, respectively.

To apply a fit with Eq. (5), we first need to validate that there are either flat bands or bands with opposite slopes in the phonon dispersion that can account for anharmonic decay channels consisting of a combination of two phonons with different energies, ω_1 and ω_2, with a sum equal to the Raman energy of the mode under analysis. A more thorough approach consists of calculating the two-phonon DOS corresponding to sum modes and searching for Van Hove singularities at the

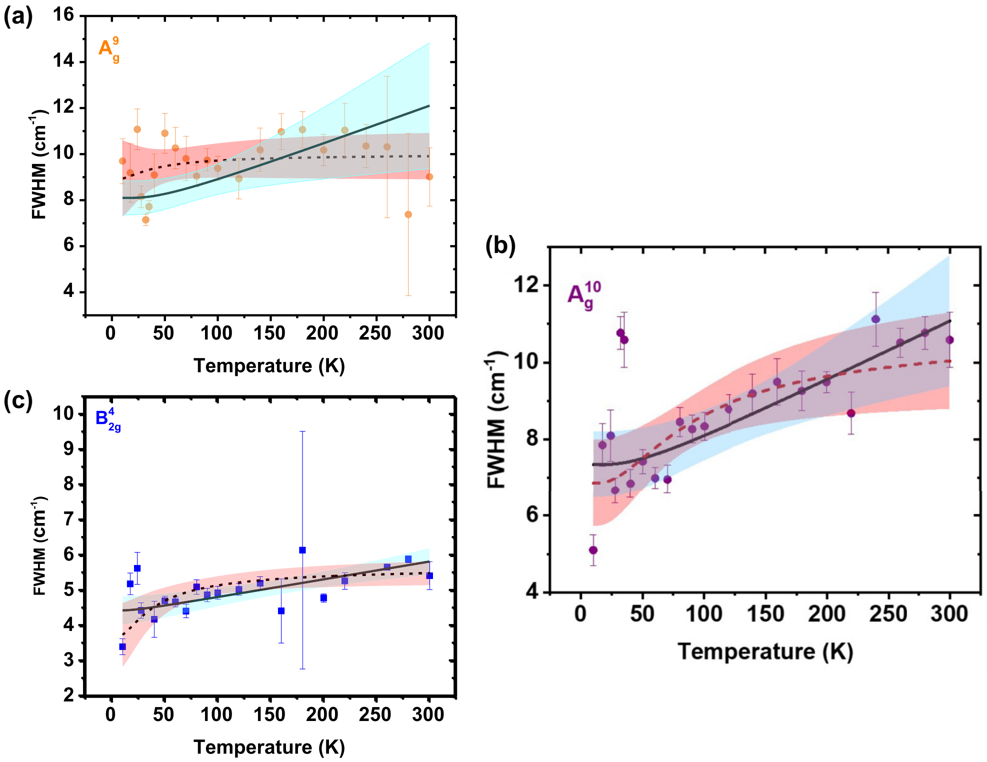

FIG. 6. Temperature dependence of the intrinsic phonon FWHM of the o-Bi_2Se_3 Raman modes corresponding to (a) $\omega_0 = 164$ cm^{-1} (A_g^9), (b) $\omega_0 = 180$ cm^{-1} (A_g^{10}), and (c) $\omega_0 = 76$ cm^{-1} (B_{2g}^4). The solid line displays fits with Eq. (4) whereas the dashed lines indicate a fit with a decay channel of two phonons of different energies [70] using Eq. (5). A much better fit is obtained in (a) and (c) with the latter equation. However, in (b) both fits display a similar quality, revealing the need to be cautious with these fits. Color bands have been used to show the 99 confidence interval [64].

Raman energies [63,71]. Due to constraints of the program we used to obtain our *ab initio* phonon energies, this option was not available.

Visual inspection of the phonon dispersion relations reveals combinations of flat bands of acoustic and optic modes that can yield more likely decay channels for the three Raman modes mentioned above. Thus, e.g., for A_g^{10}, $\omega_0 = 180.5$ cm^{-1}, we take $\omega_1 = 67.5$ cm^{-1} and $\omega_2 = 113$ cm^{-1}, that correspond to flat phonon dispersions along the U-R high symmetry direction. Similarly, for B_{2g}^4, $\omega_0 = 76$ cm^{-1}, we can assign $\omega_1 = 25$ cm^{-1} and $\omega_2 = 51$ cm^{-1}, corresponding to the flat phonon dispersion along the Z-U high symmetry direction. For A_g^9, $\omega_0 = 164$ cm^{-1}, a similar argument can be employed using a combination of modes located at 55 cm^{-1} and 109 cm^{-1}, i.e., corresponding to two maxima of the one-phonon DOS due to flat dispersions along the S-Y direction, among others. Note that these choices correspond roughly to $\omega_1 = 0.33\ \omega_0$ and $\omega_2 = 0.66\ \omega_0$, similar to the values used in Ref. [70] to obtain an accurate description of the Raman phonon linewidths for silicon.

The linewidth values plotted in Fig. 6 have been obtained after deconvolution of the Raman peak, in a similar way as described in Ref. [46]. Table V displays the values obtained for the fitting parameters of Eqs. (4) and (5) to the displayed modes: B_{2g}^4, A_g^9, and A_g^{10}. Color bands have been added to show the 99% confidence interval and ascertain the quality of both fits. Whereas both equations yield relatively good fits for the B_{2g}^4 mode, and similar values for defect- and anharmonic-attributed broadening for A_g^9, they seem to disagree in the description of the A_g^{10} phonon linewidth. Klemens's equation tends to give more weight to the contribution of disorder and defects in the linewidth, while Menéndez and Cardona's equation reveals a larger anharmonic effect. This calls for caution when using these equations to infer the extent of either contribution to the broadening. Since Eq. (5) takes into account implicitly both overtones and combinations

TABLE V. Inhomogeneous (Γ_0) and anharmonic (Γ_1) contributions to the phonon linewidth of the Raman modes displayed in Fig. 6, obtained using Eqs. (4) and (5), taking into account the error bars in both fits. Note that, for A_g^{10}, fits with both equations yield nearly the same quality, reduced Chi-square values equal to 7.04 and 7.63, respectively, leading to different relative weight of both contributions.

Mode	Γ_0 (cm^{-1})	Γ_1 (cm^{-1})
B_{2g}^4 [Eq. (4)]	4.3(2)	0.14(2)
B_{2g}^4 [Eq. (5)]	1.7(7)	2.0(4)
A_g^9 [Eq. (4)]	7.0(5)	1.1(3)
A_g^9 [Eq. (5)]	7.8(15)	1.1(9)
A_g^{10} [Eq. (4)]	6.3(5)	1.0(2)
A_g^{10} [Eq. (5)]	2.8(12)	4.0(9)

of phonons, a more accurate description than that of Klemens's, when both fits have a similar quality, we recommend choosing Menéndez and Cardona's formalism [70].

Following this line of argumentation, the higher value of Γ_1, 4.0(9) cm^{-1}, observed for the higher frequency mode, A_g^{10}, compared to that obtained for the B_{2g}^4 mode [$\Gamma_1 = 2.0(4)$ cm^{-1}], agrees with the larger anharmonic effects in the phonon frequency observed also for this mode. This can be attributed to a larger value of the two-phonon density of states, since there is also a critical point in the phonon band structure at both 36 cm^{-1} and 144 cm^{-1} that may yield another suitable decay channel for the A_g^{10} mode.

Further modes have been analyzed with no relevant changes to the conclusions of the paper, and their main results are shared in the Supplemental Material [24]. It is worth noting that different modes exhibit different temperature dependencies both in the linewidth and in the Raman shift due to varying decay channels and anharmonic coupling matrix elements [62,70].

V. CONCLUSIONS

We have reported here the temperature dependence of the Raman spectrum of orthorhombic, *Pnma*, Bi_2Se_3 in the 10 K–300 K temperature range and analyzed the Raman shifts using a two-oscillator Klemens-like model. The Raman shifts at 10 K are in agreement with the predictions we obtained using linear-response *ab initio* calculations. An anomalous anharmonic behavior is observed in the temperature dependence of the phonon linewidths for at least two of the Raman modes, displaying a two-slope trend with increasing temperature. This can be attributed to a combination of large defect concentration and significant anharmonic effects. More experimental work with additional samples should be done to ascertain the weight of each contribution. We have also observed by cathodoluminescence a lower limit of 0.835 eV for the electronic band gap energy of o-Bi_2Se_3. The band gap seems to have an indirect nature, given the low intensity observed in the experimental data, and also in agreement with both our calculations and those previously reported using the *GW* approximation. These results shed light on some of the fundamental properties of orthorhombic Bi_2Se_3, a metastable material of interest for applications in thermoelectrics.

ACKNOWLEDGMENTS

This work is financed by the Spanish Ministerio de Ciencia e Innovación and the Agencia Estatal de Investigación MCIN/AEI/10.13039/501100011033 as part of the project MALTA Consolider Team Network (RED2022-134388-T), and I+D+i Projects No. PID2019-106383GB-42/43, No. PID2021-126046OB-C22, No. TED2021-130786B-I00 also funded by MTED, and No. PID2022-138076NB-C42/C44 cofinanced by EU FEDER funds. It is also funded by projects CIPROM/2021/075 (GREENMAT) and MFA/2022/025 (ARCANGEL), financed by the Generalitat Valenciana. The last project also forms part of the Advanced Materials program supported by the Spanish MCIN with funding from European Union NextGenerationEU (PRTR-C17.I1). I.M.-M. also acknowledges financial support from the European Social Fund Plus, Operational Program of Castilla y Leon and the Junta de Castilla y Leon, Spain.

---

[1] H. Zhang, C.-X. Liu, X.-L. Qi, X. Dai, Z. Fang, and S.-C. Zhang, Topological insulators in Bi_2Se_3, Bi_2Te_3 and Sb_2Te_3 with a single Dirac cone on the surface, Nat. Phys. **5**, 438 (2009).

[2] D. Hsieh, Y. Xia, D. Qian, L. Wray, J. Dil, F. Meier, J. Osterwalder, L. Patthey, J. Checkelsky, N. Ong, A. Fedorov, H. Lin, A. Bansil, D. Grauer, Y. Hor, R. Cava, and M. Hasan, A tunable topological insulator in the spin helical Dirac transport regime, Nature (London) **460**, 1101 (2009).

[3] M. Bianchi, D. Guan, S. Bao, J. Mi, B. Iversen, P. King, and P. Hofmann, Coexistence of the topological state and a two-dimensional electron gas on the surface of Bi_2Se_3, Nat. Commun. **1**, 128 (2010).

[4] P. Cheng, C. Song, T. Zhang, Y. Zhang, Y. Wang, J.-F. Jia, J. Wang, Y. Wang, B.-F. Zhu, X. Chen, X. Ma, K. He, L. Wang, X. Dai, Z. Fang, X. Xie, X.-L. Qi, C.-X. Liu, S.-C. Zhang, and Q.-K. Xue, Landau quantization of topological surface states in Bi_2Se_3, Phys. Rev. Lett. **105**, 076801 (2010).

[5] Y. S. Hor, A. J. Williams, J. G. Checkelsky, P. Roushan, J. Seo, Q. Xu, H. W. Zandbergen, A. Yazdani, N. P. Ong, and R. J. Cava, Superconductivity in $Cu_xBi_2Se_3$ and its implications for pairing in the undoped topological insulator, Phys. Rev. Lett. **104**, 057001 (2010).

[6] H. Peng, K. Lai, D. Kong, S. Meister, Y. Chen, X. Qi, S.-C. Zhang, Z. Shen, and Y. Cui, Aharonov-Bohm interference in topological insulator nanoribbons, Nat. Mater. **9**, 225 (2010).

[7] C. Li, O. van 't Erve, J. Robinson, Y. Liu, L. Li, and B. Jonker, Electrical detection of charge-current-induced spin polarization due to spin-momentum locking in Bi_2Se_3, Nat. Nanotechnol. **9**, 218 (2014).

[8] A. Mellnik, J. Lee, A. Richardella, J. Grab, P. Mintun, M. Fischer, A. Vaezi, A. Manchon, E.-A. Kim, N. Samarth, and D. Ralph, Spin-transfer torque generated by a topological insulator, Nature (London) **511**, 449 (2014).

[9] F. Katmis, V. Lauter, F. Nogueira, B. Assaf, M. Jamer, P. Wei, B. Satpati, J. Freeland, I. Eremin, D. Heiman, P. Jarillo-Herrero, and J. Moodera, A high-temperature ferromagnetic topological insulating phase by proximity coupling, Nature (London) **533**, 513 (2016).

[10] Z. Lin, Y. Liu, U. Halim, M. Ding, Y. Liu, Y. Wang, C. Jia, P. Chen, X. Duan, C. Wang, F. Song, M. Li, C. Wan, Y. Huang, and X. Duan, Solution-processable 2D semiconductors for high-performance large-area electronics, Nature (London) **562**, 254 (2018).

[11] S. Mishra, S. Satpathy, and O. Jepsen, Electronic structure and thermoelectric properties of bismuth telluride and bismuth selenide, J. Phys.: Condens. Matter **9**, 461 (1997).

[12] Y. S. Hor, A. Richardella, P. Roushan, Y. Xia, J. G. Checkelsky, A. Yazdani, M. Z. Hasan, N. P. Ong, and R. J. Cava, *p*-type Bi_2Se_3 for topological insulator and low-temperature thermoelectric application, Phys. Rev. B **79**, 195208 (2009).

[13] G. Snyder and E. Toberer, Complex thermoelectric materials, Nat. Mater. **7**, 105 (2008).

[14] T. Fang, F. Li, Y. Wu, Q. Zhang, X. Zhao, and T. Zhu, Anisotropic thermoelectric properties of *n*-type Te-free (Bi,Sb)$_2$Se$_3$ with orthorhombic structure, ACS Appl. Energy Mater. **3**, 2070 (2020).

[15] K. Klösel, C. Roman, and C. Hierold, Thermoelectric and thermoresistive effect in Bi$_2$Se$_3$: A novel dual-mode temperature and heat flux sensor, J. Microelectromech. Syst. **32**, 445 (2023).

[16] T. Cao and S. Wang, Topological insulator metamaterials with tunable negative refractive index in the optical region, Nanoscale Res. Lett. **8**, 526 (2013).

[17] M. Tumelero, R. Faccio, and A. Pasa, Unraveling the native conduction of trichalcogenides and its ideal band alignment for new photovoltaic interfaces, J. Phys. Chem. C **120**, 1390 (2016).

[18] S. Assali, I. Zardo, S. Plissard, D. Kriegner, M. Verheijen, G. Bauer, A. Meijerink, A. Belabbes, F. Bechstedt, J. Haverkort, and E. Bakkers, Direct band Gap wurtzite gallium phosphide nanowires, Nano Lett. **13**, 1559 (2013).

[19] J. W. Earley, Description and synthesis of the selenide minerals, Am. Mineral. **35**, 337 (1950).

[20] P. Schönherr, S. Zhang, Y. Liu, P. Kusch, S. Reich, T. Giles, D. Daisenberger, D. Prabhakaran, Y. Chen, and T. Hesjedal, A new topological insulator built from quasi one-dimensional atomic ribbons, Phys. Status Solidi RRL **9**, 130 (2015).

[21] E. Y. Atabaeva, S. A. Mashkov, and S. Popova, Crystal-structure of a new modification of Bi$_2$Se$_3$, Kristallografiya **18**, 173 (1973).

[22] Y. Kang, Q. Zhang, C. Fan, W. Hu, C. Chen, L. Zhang, F. Yu, Y. Tian, and B. Xu, High pressure synthesis and thermoelectric properties of polycrystalline Bi$_2$Se$_3$, J. Alloys Compd. **700**, 223 (2017).

[23] C. Xiao, J. Yang, W. Zhu, J. Peng, and J. Zhang, Electrodeposition and characterization of Bi$_2$Se$_3$ thin films by electrochemical atomic layer epitaxy (ECALE), Electrochim. Acta **54**, 6821 (2009).

[24] See Supplemental Material at http://link.aps.org/supplemental/10.1103/PhysRevB.111.134304 for additional information regarding X-ray diffraction and Raman scattering data and analysis.

[25] N. Serebryanaya, R. Bagramov, S. Buga, I. Pahomov, N. Eliseev, and V. Blank, New metastable phase of bismuth (III) selenide: Crystal structure and electrical properties, Phys. Status Solidi (b) **257**, 2000145 (2020).

[26] J. Rodríguez-Carvajal, Recent developments of the program FULLPROF, in commission on powder diffraction, IUCr Newsl. **26**, 12 (2001).

[27] F. Manjón, S. Gallego-Parra, P. Rodríguez-Hernández, A. Muñoz, C. Drasar, V. Muñoz-Sanjosé, and O. Oeckler, Anomalous Raman modes in tellurides, J. Mater. Chem. C **9**, 6277 (2021).

[28] P. Hohenberg and W. Kohn, Inhomogeneous electron gas, Phys. Rev. **136**, B864 (1964).

[29] G. Kresse and J. Fürthmuller, Efficient iterative schemes for *ab initio* total-energy calculations using a plane-wave basis set, Phys. Rev. B **54**, 11169 (1996).

[30] P. E. Blöchl, Projector augmented-wave method, Phys. Rev. B **50**, 17953 (1994).

[31] G. Kresse and D. Joubert, From ultrasoft pseudopotentials to the projector augmented-wave method, Phys. Rev. B **59**, 1758 (1999).

[32] J. P. Perdew, K. Burke, and M. Ernzerhof, Generalized gradient approximation made simple, Phys. Rev. Lett. **77**, 3865 (1996).

[33] S. Grimme, J. Antony, S. Ehrlich, and S. Krieg, A consistent and accurate *ab initio* parametrization of density functional dispersion correction (DFT-D) for the 94 elements H-Pu, J. Chem. Phys. **132**, 154104 (2010).

[34] Y. Hinuma, G. Pizzi, Y. Kumagai, F. Oba, and I. Tanaka, Band structure diagram paths based on crystallography, Comput. Mater. Sci. **128**, 140 (2017).

[35] M. Tumelero, L. Benetti, E. Isoppo, R. Faccio, G. Zangani, and A. Pasa, Electrodeposition and *ab initio* studies of metastable orthorhombic Bi$_2$Se$_3$: A novel semiconductor with bandgap for photovoltaic applications, J. Phys. Chem. C **120**, 11797 (2016).

[36] A. Togo and I. Tanaka, First principles phonon calculations in materials science, Scr. Mater. **108**, 1 (2015).

[37] R. Caracas and X. Gonze, First-principles study of the electronic properties of A$_2$B$_3$ minerals, with A=Bi,Sb and B=S,Se, Phys. Chem. Minerals **32**, 295 (2005).

[38] Y. Sharma and P. Srivastava, First-principles study of electronic and optical properties of Bi$_2$Se$_3$ in its trigonal and orthorhombic phases, AIP Conf. Proc. **1249**, 183 (2010).

[39] M. R. Filip, C. E. Patrick, and F. Giustino, *GW* quasiparticle band structures of stibnite, antimonselite, bismuthinite, and guanajuatite, Phys. Rev. B **87**, 205125 (2013).

[40] P. Souza, M. Tumelero, R. Faccio, R. Ahmed, C. P. Cid, G. Zangari, and A. Pasa, Vibrational properties of metastable orthorhombic Bi$_2$Se$_3$, Phys. Chem. Chem. Phys. **25**, 14440 (2023).

[41] N. Fleck, T. Hobson, C. Savory, J. Buckeridge, T. Veal, M. Correia, D. Scanlon, K. Durose, and F. Jäckel, Identifying Raman modes of Sb$_2$Se$_3$ and their symmetries using angle-resolved polarised Raman spectra, J. Phys. Chem. A **8**, 8337 (2020).

[42] J. Ibáñez, J. Sans, C. Popescu, J. López-Vidrier, J. Elvira-Betanzos, V. Cuenca-Gotor, O. Gomis, F. Manjón, P. Rodríguez-Hernández, and A. Muñoz, Structural, vibrational, and electronic study of Sb$_2$S$_3$ at high pressure, J. Phys. Chem. C **120**, 10547 (2016).

[43] R. Vilaplana, D. Santamaría-Pérez, O. Gomis, F. J. Manjón, J. González, A. Segura, A. Muñoz, P. Rodríguez-Hernández, E. Pérez-González, V. Marín-Borrás, V. Muñoz-Sanjosé, C. Drasar, and V. Kucek, Structural and vibrational study of Bi$_2$Se$_3$ under high pressure, Phys. Rev. B **84**, 184110 (2011).

[44] M. Deshpande, S. Bhatt, V. Sathe, R. Rao, and S. Chaki, Pressure and temperature dependence of Raman spectra and their anharmonic effects in Bi$_2$Se$_3$ single crystal, Phys. B: Condens. Matter **433**, 72 (2014).

[45] M. Eddrief, P. Atkinson, V. Etgens, and B. Jusserand, Low-temperature Raman fingerprints for few-quintuple layer topological insulator Bi$_2$Se$_3$ films epitaxied on GaAs, Nanotechnology **25**, 245701 (2014).

[46] S. Buchenau, S. Scheitz, A. Sethi, J. E. Slimak, T. E. Glier, P. K. Das, T. Dankwort, L. Akinsinde, L. Kienle, A. Rusydi, C. Ulrich, S. L. Cooper, and M. Rübhausen, Temperature and magnetic field dependent Raman study of electron-phonon interactions in thin films of Bi$_2$Se$_3$ and Bi$_2$Te$_3$ nanoflakes, Phys. Rev. B **101**, 245431 (2020).

[47] W. Richter, H. Köhler, and C. Becker, A Raman and far-infrared investigation of phonons in the rhombohedral V_2VI_3 compounds Bi_2Te_3, Bi_2Se_3, Sb_2Te_3 and $Bi_2(Te_{1-x}Se_x)_3$ $(0 < x < 1)$, $(Bi_{1-y}Sb_y)_2Te_3(0 < y < 1)$, Phys. Status Solidi (b) **84**, 619 (1977).

[48] J. Zhang, Z. Peng, A. Soni, Y. Zhao, Y. Xiong, B. Peng, J. Wang, M. Dresselhaus, and Q. Xiong, Raman spectroscopy of few-quintuple layer topological insulator Bi_2Se_3 nanoplatelets, Nano Lett. **11**, 2407 (2011).

[49] V. Gnezdilov, Y. G. Pashkevich, H. Berger, E. Pomjakushina, K. Conder, and P. Lemmens, Helical fluctuations in the Raman response of the topological insulator Bi_2Se_3, Phys. Rev. B **84**, 195118 (2011).

[50] D. Sharma, M. Sharma, R. Meena, and V. Awana, Raman spectroscopy of $Bi_2Se_{3-x}Te_x$ topological insulator crystals, Phys. B: Condens. Matter **600**, 412492 (2021).

[51] D. Rawat, A. Singh, N. K. Singh, and A. Soni, Anisotropic light-matter interactions in the single-crystal topological insulator bismuth selenide, Phys. Rev. B **107**, 155203 (2023).

[52] K. Shahil, M. Hossain, V. Goyal, and A. Balandin, Micro-Raman spectroscopy of mechanically exfoliated few-quintuple layers of Bi_2Te_3, Bi_2Se_3, and Sb_2Te_3 materials, J. Appl. Phys. **111**, 054305 (2012).

[53] Y. Zhao, X. Luo, J. Zhang, J. Wu, X. Bai, M. Wang, J. Jia, H. Peng, Z. Liu, S. Y. Quek, and Q. Xiong, Interlayer vibrational modes in few-quintuple-layer Bi_2Te_3 and Bi_2Se_3 two-dimensional crystals: Raman spectroscopy and first-principles studies, Phys. Rev. B **90**, 245428 (2014).

[54] J. Humlíček, D. Hemzal, A. Dubroka, O. Caha, H. Steiner, G. Bauer, and G. Springholz, Raman and interband optical spectra of epitaxial layers of the topological insulators Bi_2Te_3 and Bi_2Se_3 on BaF_2 substrates, Phys. Scr. **T162**, 014007 (2014).

[55] K. Niherysh, J. Andzane, M. Mikhalik, S. Zavadsky, P. Dobrokhotov, F. Lombardi, S. Prischepa, I. Komissarov, and D. Erts, Correlation analysis of vibration modes in physical vapour deposited Bi_2Se_3 thin films probed by the Raman mapping technique, Nanoscale Adv. **3**, 6395 (2021).

[56] F. Zhou, Y. Zhao, W. Zhou, and D. Tang, Temperature-dependent Raman scattering of large size hexagonal Bi_2Se_3 single-crystal nanoplates, Appl. Sci. **8**, 1794 (2018).

[57] T. Kondo, T. Nozaki, R. Kotabe, and Y. Terai, Investigation of Raman depolarization ratio in topological insulator Bi_2Se_3 epitaxial films, Jpn. J. Appl. Phys. **62**, SD1016 (2023).

[58] B. Irfan, S. Sahoo, A. Gaur, M. Ahmadi, M.-F. Guinel, R. Katiyar, and R. Chatterjee, Temperature dependent Raman scattering studies of three dimensional topological insulators Bi_2Se_3, J. Appl. Phys. **115**, 173506 (2014).

[59] Y. Zhao, Kun Ting Eddie Chua, C. K. Gan, J. Zhang, B. Peng, Z. Peng, and Q. Xiong, Phonons in Bi_2S_3 nanostructures: Raman scattering and first-principles studies, Phys. Rev. B **84**, 205330 (2011).

[60] P. Sereni, M. Musso, P. Knoll, P. Blaha, K. Schwarz, and G. Schmidt, Polarization-dependent Raman characterization of stibnite (Sb_2S_3), AIP Conf. Proc. **1267**, 1131 (2010).

[61] P. Klemens, Anharmonic decay of optical phonons, Phys. Rev. **148**, 845 (1966).

[62] M. Balkanski, R. F. Wallis, and E. Haro, Anharmonic effects in light scattering due to optical phonons in silicon, Phys. Rev. B **28**, 1928 (1983).

[63] J. Serrano, M. Cardona, T. M. Ritter, B. A. Weinstein, A. Rubio, and C. T. Lin, Pressure and temperature dependence of the Raman phonons in isotopic γ-CuI, Phys. Rev. B **66**, 245202 (2002).

[64] A. Hazra, Using the confidence interval confidently, J. Thorac. Dis. **9**, 4124 (2017).

[65] N. K. Singh, D. Rawat, D. Dey, A. Elsukova, P. O. A. Persson, P. Eklund, A. Taraphder, and A. Soni, Electron-phonon coupling and quantum correction to topological magnetoconductivity in Bi_2GeTe_4, Phys. Rev. B **105**, 045134 (2022).

[66] A. Debernardi, S. Baroni, and E. Molinari, Anharmonic phonon lifetimes in semiconductors from density-functional perturbation theory, Phys. Rev. Lett. **75**, 1819 (1995).

[67] Y. Kim, X. Chen, Z. Wang, J. Shi, I. Miotkowski, Y. Chen, P. Sharma, A. Sharma, M. Hekmaty, Z. Jiang, and D. Smirnov, Temperature dependence of Raman-active optical phonons in Bi_2Se_3 and Sb_2Te_3, Appl. Phys. Lett. **100**, 071907 (2012).

[68] X. Yang, Z. Zhou, Y. Wang, R. Jiang, W. Zheng, and C. Sun, Raman spectroscopy determination of the Debye temperature and atomic cohesive energy of CdS, CdSe, Bi_2Se_3, and Sb_2Te_3 nanostructures, J. Appl. Phys. **112**, 083508 (2012).

[69] P. J. Graham, P. Rovillain, M. Bartkowiak, E. Pomjakushina, K. Conder, M. Kenzelmann, and C. Ulrich, Spin-phonon and magnetoelectric coupling in oxygen-isotope substituted $TbMnO_3$ investigated by Raman scattering, Phys. Rev. B **105**, 174438 (2022).

[70] J. Menéndez and M. Cardona, Temperature dependence of the first-order Raman scattering by phonons in Si, Ge, and $\alpha -$ Sn: Anharmonic effects, Phys. Rev. B **29**, 2051 (1984).

[71] J. Serrano, F. J. Manjón, A. H. Romero, F. Widulle, R. Lauck, and M. Cardona, Dispersive phonon linewidths: The E_2 phonons of ZnO, Phys. Rev. Lett. **90**, 055510 (2003).